Arch. Min. Sci. **71** (2026), 3, 455-482

Electronic version (in color) of this paper is available: http://mining.archives.pl

DOI: https://doi.org/10.24425/ams.2026.6302

QIANG FU[1], YAO HU[1], JIALE WEI[1*], KE YANG[1],
BENNIU WU[1], TONG WANG[1], QINJIE LIU[1]

PHYSICAL MODEL TEST ON DAMAGE EVOLUTION OF SURROUNDING ROCK-LINING STRUCTURE IN ABANDONED MINE COMPRESSED AIR ENERGY STORAGE CAVERNS UNDER CYCLIC LOADING

To clarify the damage evolution characteristics of the surrounding rock-lining structure under cyclic loading, a physical model testing method was adopted, focusing on the gas storage space of lined chambers in hard rock roadways in abandoned mines. A large-scale three-dimensional simulation model test system for the surrounding rock-lining structure of compressed air energy storage tunnels was developed. Conductive concrete was used as the analogous material. A multi-source monitoring system was established, including dynamic and static strain acquisition, distributed optical fibre sensing, and networked parallel electrical testing. The stress, deformation, and resistivity fields of the surrounding rock-lining structure were synchronously monitored. The results indicate that:

(1) Under the combined effects of boundary stress and excavation unloading, the vertical stress at the roof and floor of the lining and the horizontal stress at the sidewalls are progressively released from shallow to deep regions along the measurement lines. In contrast, the horizontal stress at the roof and floor and the vertical stress at the sidewalls increase synchronously, resulting in stress concentrations in the roof region and the deeper parts of the sidewalls.

(2) Under both single-stage and graded cyclic loading, the structural stress exhibits periodic fluctuations, with the response amplitude increasing as the upper limit stress rises. The regions adjacent to the lining show the most significant variations.

(3) During the excavation stage and under single-stage internal pressure, the structure is primarily characterised by compressive deformation, with more pronounced compression at the sidewalls than at the roof and floor. As the upper limit stress of graded cyclic loading increases, the deformation gradually transitions from compression to tension. When the stress exceeds 1.0 MPa, the peak tensile strain at the roof and floor reaches 700-1000 με, accompanied by significant non-uniform deformation.

(4) Apparent resistivity results demonstrate that, with increasing upper-limit stress, microcracks within the lining progressively propagate, leading to the formation of high-resistivity damage zones in the roof, floor, and shallow sidewall regions. These changes effectively reflect the

[1] ANHUI UNIVERSITY OF SCIENCE AND TECHNOLOGY, CHINA

* Corresponding author: wjl8911@aust.edu.cn

© 2026. The Author(s). This is an open-access article distributed under the terms of the Creative Commons Attribution License (CC-BY 4.0). The Journal license is: https://creativecommons.org/licenses/by/4.0/deed.en. This license allows others to distribute, remix, modify, and build upon the author's work, even commercially, as long as the original work is attributed to the author.

damage evolution process of the structure. The findings provide a basis for understanding the macroscopic stress redistribution, deformation behaviour, and failure mechanisms of surrounding rock-lining systems in gas storage roadways of compressed air energy storage power stations under cyclic loading.

Keywords: Abandoned mines; compressed air energy storage; surrounding rock-lining structure; cyclic loading; model test; damage evolution

1. Introduction

With the continuous increase in China's energy demand and the accelerated development of deep coal resources, a significant number of abandoned mine resources require efficient reutilisation, among which underground compressed air energy storage (CAES) has demonstrated significant application potential. However, the bearing characteristics and damage mechanisms of the surrounding rock-lining structures in abandoned mine gas storage roadways under cyclic loading remain unclear, and systematic investigations are urgently needed [1,2]. As an important approach for studying the stress distribution and deformation characteristics of surrounding rock in underground engineering, physical model testing can reproduce in situ stress conditions, construction processes, and complex loading scenarios under controlled laboratory conditions. Compared with numerical simulation methods, physical model tests can not only reproduce the macroscopic mechanical responses of structures under various working conditions but also directly reveal the progressive evolution of surrounding rock behaviour from elastic-plastic deformation, crack initiation and propagation, to final damage and failure, thereby providing an important basis for understanding the instability mechanisms of underground structures [3,4]. For compressed air energy storage roadways, the stress evolution process is not characterised by monotonic loading but by repeated charging and discharging cycles, continuous stress redistribution, and cumulative residual effects. Therefore, the focus of physical model testing should extend beyond deformation and failure behaviour under peak loading conditions and should also address the nonlinear evolution mechanisms during cyclic loading, including stress transfer pathways, tension-compression state transitions, residual deformation accumulation, and damage localisation.

Similarity theory provides the theoretical foundation for physical model testing. By applying the three fundamental similarity criteria, namely geometric similarity, physical similarity, and boundary condition similarity, a quantitative mapping relationship between the model and prototype can be established, thereby providing theoretical support for the reliable extrapolation of experimental results to engineering applications [5,6]. Similar simulation testing is one of the important approaches for investigating mining-related engineering problems. Since similar simulation technology was introduced into China in the 1960s, it has been widely applied in studies of mining, surrounding rock control, and underground structure stability, gradually evolving from qualitative analysis toward quantitative investigation. In recent years, extensive studies have been conducted by researchers worldwide on surrounding rock pressure distribution, deformation characteristics, and support structure responses by integrating similar simulation, numerical analysis, and field monitoring methods [7-10]. These studies have revealed the deformation and failure mechanisms of tunnels and underground caverns under high in situ stress conditions, analysed the stress and displacement responses of gas storage structures subjected to different in situ stress states and charging-discharging conditions, and provided preliminary experimental support for the

application of soft rock roadways in compressed air energy storage projects [11-14]. Furthermore, the integration of distributed optical fibre sensing and electrical monitoring technologies with similarity simulation tests has provided a new technical approach for quantitatively identifying fracture evolution processes [15]. Most existing studies have focused on regular underground caverns, single surrounding rock media, or independent lining structures. However, insufficient attention has been paid to the surrounding rock-lining composite structures of abandoned mine roadways with initial disturbance characteristics, and the transfer and redistribution mechanisms of alternating internal pressure between the lining and surrounding rock have not yet been fully understood. Furthermore, most existing experimental studies have focused on static loading, monotonic loading, or limited condition comparisons, mainly examining the stress response, displacement characteristics, and failure modes at specific loading stages. A systematic understanding of the relationships among response amplitude variation, residual effect accumulation, local tension-compression state transitions, and progressive damage evolution throughout cyclic loading remains lacking. In addition, existing studies generally rely on single or limited monitoring parameters, such as strain, displacement, or fracture observations. Different types of monitoring data are mostly treated as independent measurements, and the synchronous coupling relationships among stress redistribution, structural deformation, fracture propagation, and electrical parameter variations have not been fully established. Therefore, although previous studies have revealed the periodic response characteristics and local stress concentration behaviour of gas storage structures under charging-discharging operations, clear experimental evidence is still lacking regarding how these macroscopic responses evolve into the degradation of the collaborative bearing capacity of surrounding rock-lining systems and how continuously monitored physical parameters can be used to identify damage initiation and development processes.

In similarity simulation tests, the physical and mechanical properties of similar materials, including density, strength, and elastic modulus, directly determine the similarity relationship of the model and the reliability of experimental results. Therefore, the rational design of material composition and proportion is essential for ensuring test accuracy. Currently, orthogonal experimental design methods have been widely applied in the optimisation of similar material mixtures. Through multi-factor and multi-level combination tests, the effects of sand, gypsum, cement, and barite on material properties have been systematically investigated. Regression analysis has been employed to establish performance prediction models for similar materials with different strength grades [16-20]. Meanwhile, advanced experimental design approaches, such as the response surface method, have gradually been introduced into similar material research, effectively revealing the nonlinear coupling relationships among multiple influencing factors and improving the accuracy of mixture optimisation [21].

Furthermore, considering the characteristics of soft rock and coal-rock materials, some researchers have enhanced the mechanical properties of similar materials and enabled real-time monitoring of internal damage evolution by introducing composite binders or functional materials (carbon fibres), providing new approaches for multi-field coupled monitoring [22-25]. However, existing studies on similar functional materials have mainly focused on material property regulation or the feasibility validation of electrical responses. The quantitative relationship between resistivity variations and internal stress transfer, tension-compression state transitions, and crack propagation within complex structures remains unclear. In particular, systematic investigations into the mechanical-electrical synergistic characterisation of surrounding rock-lining composite structures under cyclic loading are still lacking.

Based on the above considerations, this study develops a large-scale three-dimensional physical model testing system for investigating the damage and instability behaviour of surrounding rock-lining structures in compressed air energy storage roadways. Conductive concrete-like materials were prepared, and their mixture proportions were optimised through orthogonal experimental design. A series of model tests were conducted to investigate the mechanical response of gas storage roadways under cyclic loading conditions. By integrating multi-source monitoring techniques, including dynamic and static strain measurement, distributed optical fibre sensing, and electrical resistivity monitoring, the synergistic characterisation of stress, deformation, and resistivity evolution in the surrounding rock-lining structure was achieved. Furthermore, the micro-damage mechanism of conductive concrete under loading was revealed, and the evolution of bearing capacity as well as the damage and failure characteristics of surrounding rock-lining structures under cyclic loading were systematically investigated. The results provide a foundation for understanding the macroscopic stress redistribution, deformation behaviour, and failure mechanisms of surrounding rock-lining systems in compressed air energy storage power stations subjected to cyclic loading.

2. Physical simulation experiment

2.1. Construction of the experimental system

Utilising the multifunctional three-dimensional similarity simulation platform at Anhui University of Science and Technology, a large-scale three-dimensional model test system was independently designed and constructed to investigate the damage and instability of surrounding rock-lining structures in hard-rock gas storage chambers. This experimental setup allows the concurrent application of internal and external loads, which can be flexibly adjusted to match different simulation conditions, facilitating the physical simulation of damage evolution and instability in the surrounding rock of gas storage chambers under diverse combined loading conditions. The experimental setup comprises four main components: a multifunctional simulation platform, a hydraulic loading and control system, an internal pressure loading apparatus, and a multi-source data acquisition system. A detailed description of each component is provided below (Fig. 1):

(1) The multifunctional simulation platform utilises a hydraulic loading system to implement triaxial gradient loading along the top, lateral, and rear directions. The applied pressures can be precisely controlled within a range of 0 to 2.25 MPa, with load fluctuations maintained below 5%. The platform is also fitted with removable thrust plates and observation windows to facilitate the integration of the internal pressure loading apparatus.

(2) The hydraulic loading control system is composed of a pump station, an accumulator, proportional valves, and a computer control unit. It enables multi-level sectional pressurisation and fully automated control, providing real-time pressure monitoring and adjustment capabilities.

(3) The internal pressure loading apparatus consists of a high-pressure airbag and an arc-shaped steel hydraulic jack, allowing precise simulation of the internal pressure within the gas storage chamber. The system features a maximum air discharge rate of 600 L/min, an operating pressure of 0.8 MPa, a tank volume of 120 L, and a cylinder diameter of

90 mm. The high-pressure airbag is fabricated from premium composite nitrile rubber and polymer materials using a high-temperature vulcanisation process, providing excellent wear and heat resistance, and is capable of withstanding a maximum pressure of 0.8 MPa. The digitally controlled pressure gauge comprises a high-pressure rubber hose, an LCD, and an external metal air charging/discharging valve, providing accurate pressure measurements during manual charging and discharging with an error below 1%. The hydraulic jack features a rated capacity of 30 T, a cylinder internal diameter of 80 mm, and a 14 mm stroke, and the electric hydraulic pump can generate a maximum pressure of 70 MPa.

(4) A multi-source monitoring system was implemented to characterise the stress, strain, and crack evolution of surrounding rock-lining structures under cyclic loading. Stress measurements were obtained using polyurethane strain bricks and miniature earth pressure cells integrated with a multi-channel acquisition system. Data were collected using the TML multi-channel strain measurement system (Tokyo Sokki, Japan) with a sampling frequency of 1 Hz. Strain measurements were carried out using the TML multi-channel strain measurement system (Tokyo Sokki, Japan) in conjunction with the fTB-2505 distributed optical fibre monitoring system, allowing for high-resolution reconstruction of the strain field. Crack evolution was monitored through the NPEI-DHZI networked parallel electrical measurement system, which facilitated inversion of internal fracture development. The system enables the simultaneous acquisition of multi-source physical information, supplying critical experimental data for studying the damage mechanisms and instability patterns of surrounding rock-lining structures in gas storage chambers under the coupled effects of internal and external stresses.

The test system is characterised by its ability to replicate realistic in situ stress environments, implement digitally controlled internal pressure loading, and simultaneously monitor multi-source physical data in real time. It provides a robust experimental platform for evaluating the safety and optimising the operation of surrounding rock-lining structures in hard-rock gas storage caverns.

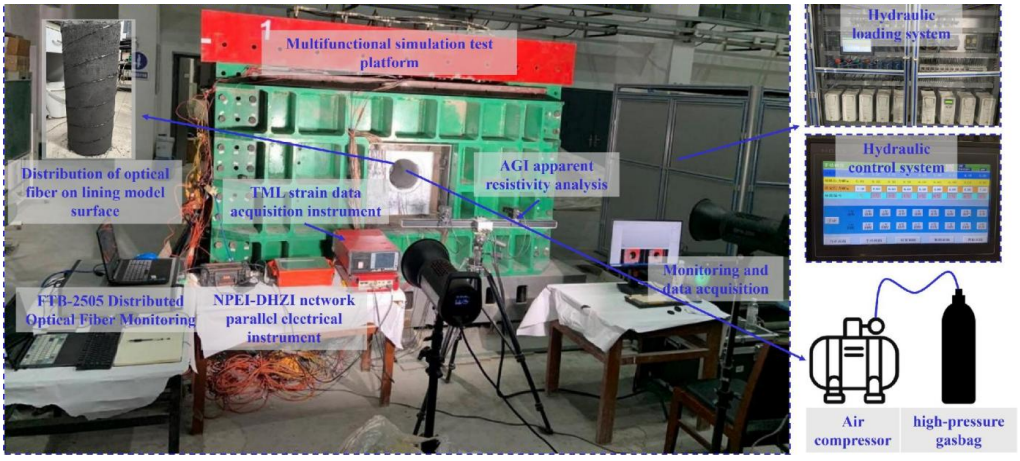

Fig. 1. Large-scale three-dimensional hard rock tunnel lining chamber gas storage space surrounding rock-lining structure damage and instability model test system

2.2. Design of the model test

Based on the geological and engineering conditions of a development roadway in a deep mine in Huainan, Anhui Province, the dimensions of the three-dimensional physical model were determined as 200 cm × 140 cm × 70 cm. The prototype roadway adopts a straight wall semi-circular arch section, with a straight wall height of 2 m, an arch radius of 2.5 m, and a burial depth ranging from 800 m to 810 m. Considering the actual engineering conditions and internal pressure loading requirements, the prototype roadway was further simplified into a circular section with a diameter of 5 m for the model test.

According to similarity theory, the geometric, stress, and bulk density similarity ratios of the model were determined as 0.05, 0.04, and 0.8, respectively. The detailed parameter determination process is as follows. Considering the influence range of the surrounding rock mass around the roadway, the geometric similarity ratio was selected as C_D = 1:20. Combined with the bulk density range achievable by the self-developed similar materials for surrounding rock, and to ensure similarity of the self-weight stress field, the bulk density similarity ratio of the surrounding rock was determined as $C_{\gamma\text{-}Rock}$ = 1:1.25 [16,17]. After extensive development of model testing techniques in mining engineering, a relatively well-established stress similarity framework has been formed. According to similarity theory, the stress similarity ratio can be expressed as:

$$C_\sigma = C_\gamma C_D \tag{1}$$

where C_σ, C_γ, and C_D represent the similarity ratios of stress, bulk density, and geometry, respectively.

$$C_D = C_\sigma C_\varepsilon \tag{2}$$

where C_δ and C_ε denote the displacement and strain similarity ratios, respectively.

$$C_E = C_\sigma C_\varepsilon \tag{3}$$

where C_E is the elastic modulus similarity ratio.

In addition, because the internal friction angle (β), friction coefficient (μ), strain (ε), and Poisson's ratio (v) of the model and prototype were kept identical, their similarity ratios were all taken as 1.

$$C_\varepsilon = 1,\ C_\beta = 1,\ C_\mu = 1,\ C_v = 1 \tag{4}$$

According to Equations (1)-(3), the following relationships can be obtained.

$$C_\sigma = C_E = C_c = C_{\sigma_c} = C_{\sigma_t} \tag{5}$$

Therefore, the similarity ratios of stress and elastic modulus are:

$$C_\sigma = C_E = C_\gamma C_D = 25 \tag{6}$$

and the time similarity ratio is:

$$C_t = \sqrt{C_D} \approx 4.5 \tag{7}$$

The in-situ stress distribution within the rock mass surrounding a development roadway with an average burial depth of 805 m was determined using the hollow inclusion stress relief

technique. The strain values measured by the inclusions during the stress relief process are presented in Fig. 2. The principal stress magnitudes and their orientations in the area surrounding the roadway were determined and are presented in TABLE 1. The determined principal stresses σ_1, σ_2, and σ_3 were resolved along the horizontal, axial, and vertical directions of the roadway model, providing the corresponding prototype loads necessary for the calculation of model loading. The specific values were 16.57 MPa, 22.32 MPa, and 19.51 MPa for the respective directions. Accordingly, using the established similarity ratios, the stress boundary conditions applied to the model in the vertical (σ_z), horizontal (σ_x), and axial (σ_y) directions were determined to be 0.78 MPa, 0.66 MPa, and 0.90 MPa, respectively.

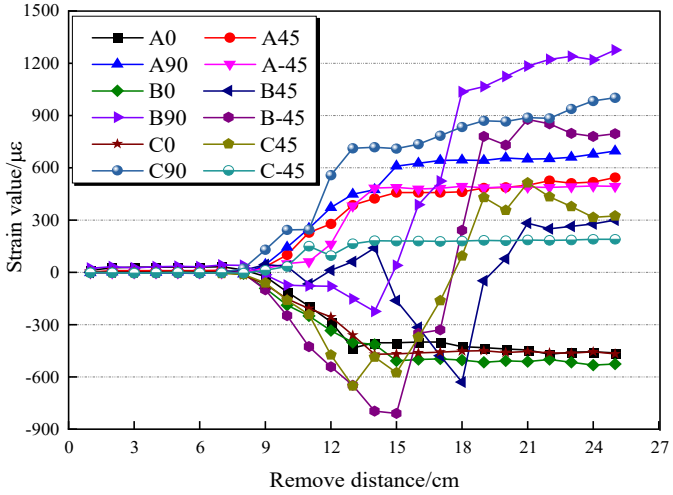

Fig. 2. Stress relief process curve

TABLE 1

Magnitude and orientation of principal stress

Principal stress	Stress (MPa)	Azimuth angle (°)	Dip angle (°)	Stress distribution diagram
σ_1	21.63	NE98.3	19.75	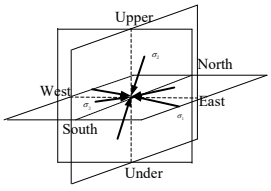
σ_2	19.28	NE22.8	85.1	
σ_3	15.63	NE17.1	30.5	

2.3. Selection of similar materials and optimisation of mix proportions

Conductive concrete is a multiphase composite comprising cementitious materials, conductive additives, aggregates, and water, engineered to exhibit both predetermined electrical

conductivity and tailored mechanical properties. It finds broad application in cold-region infrastructure, including dam-surface deicing [26], roadway deicing [27], and building interior heating [28]. Considerable research has been conducted internationally on its material composition, electrical conductivity, heating performance, mechanical behaviour, and impermeability characteristics [29-31]. Researchers have found that the inclusion of conductive additives in cement-based materials establishes continuous conductive networks within the concrete, endowing it with the ability to self-sense deformation and damage. Under applied loads, a correlation emerges between the concrete's electrical resistivity and stress, offering a promising method for real-time monitoring of structural integrity and operational state [32-34]. Moreover, conductive concrete is easily accessible, economically favourable, and demonstrates excellent durability, making it a practical choice for engineering applications. In conclusion, the piezoresistive behaviour of conductive concrete offers a feasible approach for monitoring the mechanical response of models under applied loads and for investigating structural stability under cyclic loading. This material not only allows intuitive visualisation of model changes during loading and excavation but also facilitates detailed observation of internal structural evolution through its sensitive piezoresistive response and energy release characteristics during deformation and fracture.

The strength of similar materials should be comprehensively determined according to the properties of the prototype material and similarity ratios, rendering conventional conductive concrete mix designs inapplicable. Consequently, a systematic study on the mix design of conductive concrete for use as a similar material is required. To satisfy the requirements of three-dimensional similitude modelling and rapidly determine accurate mix proportions for guiding the layering of model rock strata, an orthogonal experimental approach was applied. Coal gangue and river sand (aggregates), cement and fly ash (binders), and graphite powder and steel fibres (conductive materials) were proportionally blended to fabricate standard concrete specimens, which were then tested to determine their strength and obtain the target mix. The factors and levels used in the orthogonal design of the conductive concrete similar material are listed in TABLE 2.

TABLE 2

Factors and levels of similar simulated material proportioning experiments based on conductive concrete

Level	Factor				
	A (Aggregate / Cementitious)	**B (Gelation / Conductive)**	**C (Cement / Fly ash)**	**D (Graphite / Steel fibre)**	**E (Water content)**
1	5:1	25:1	3:7	12:1	0.15
2	7.5:1	20:1	4:6	12:2	0.175
3	10:1	15:1	5:5	12:3	0.20
4	12.5:1	10:1	6:4	12:4	0.225
5	15:1	5:1	7:3	12:5	0.25

For the mix design experiments, each factor was assigned five levels, and an L25(5^6) orthogonal array was employed. The five factors considered were: A, the mass ratio of aggregates to binder; B, the mass ratio of binder to conductive materials; C, the mass ratio of cement to fly

ash; D, the mass ratio of graphite powder to steel fibres; and E, the water-to-total material mass ratio (water content).

In the mix design experiments, three standard specimens were prepared for each of the 25 mix schemes presented in Table 2. For each batch, the quantities of coal gangue, fine river sand, cement, fly ash, graphite powder, steel fibres, and water were calculated, accurately weighed, and homogeneously mixed. The mixtures were cast into 70 mm × 70 mm × 70 mm plastic cube moulds and compacted by vibration, yielding a total of 75 specimens. Following demolding, the prepared specimens were cured in a controlled environment chamber at 25°C and 95% relative humidity for 15 days. After curing, key physical properties, including bulk density, were measured for each group. Uniaxial compression tests were performed on all mix-design specimens using an RMT150B rigid testing machine to record compressive strength. Electrical resistivity changes were monitored using a CXT5511 resistivity tester (Changzhou Xinyang Electronics Co., Ltd.) employing the Kelvin method, with brass electrodes affixed to the top and bottom surfaces of each specimen and a measurement frequency of 1 Hz. Fig. 3 illustrates the preparation of the mix-design specimens, the uniaxial compression testing process, and the resulting failure modes of the specimens.

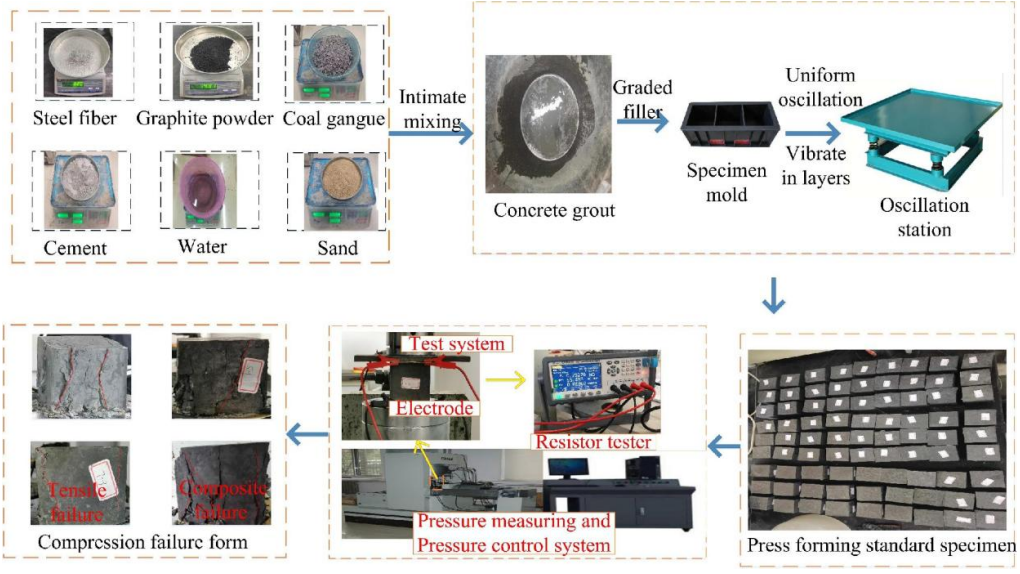

Fig. 3. Flow chart of conductive concrete material proportioning test

To characterise the physical and mechanical properties of the crown and invert surrounding rock, cores were taken from the arch shoulders and crown/invert and prepared into standard specimens measuring ϕ50 mm × 100 mm, ϕ50 mm × 25 mm, and ϕ50 mm × 50 mm. The bulk density of each specimen was determined, and uniaxial compressive, tensile, and shear strengths were measured to obtain the physical and mechanical parameters of the surrounding rock, as presented in TABLE 3.

TABLE 3

Physical and mechanical parameters of surrounding rock of roadway

Lithology	Thickness / m	Volume weight /(kN/m^3)	Compressive strength /MPa	*E* /GPa	Cohesion /MPa	Internal friction angle /(°)	Poisson ratio
Siltstone	20	26.51	61.75	13.03	2.56	38	0.20
Fine sandstone	10	24.45	44.83	9.87	2.31	31	0.22
Silty fine sandstone	10	25.91	52.52	11.23	2.42	32	0.22

Using the physical and mechanical properties of the surrounding rock and C30 concrete lining as a basis, bulk density and compressive strength were selected as similitude matching parameters to define the mix design. Combined with the previously determined similarity constants, the original and target values of the similitude parameters for four lithologies-fine sandstone, siltstone, sandy siltstone, and lining concrete-were established, as presented in TABLE 4.

TABLE 4

Matching parameters of volume weight and strength of different lithologies

Lithology		Siltstone	Fine sandstone	Silty fine sandstone	Concrete lining
Volume weight /(kN/m^3)	Original parameters	26.51	24.45	25.91	23.95
	Target parameter	21.21	19.56	20.73	19.16
Compressive strength /MPa	Original parameters	61.75	44.83	52.52	26.51
	Target parameter	2.47	1.79	2.10	1.06

Fig. 4 presents the matching of similar materials for physical models representing four lithologies: fine sandstone, siltstone, sandy siltstone, and lining concrete. Figure 4 indicates that the target compressive strength of siltstone closely corresponds to the experimental results of Groups 2, 4, and 5, whereas the target bulk density of siltstone is closely approximated by Groups 4, 15, and 24. The target compressive strength of fine sandstone is closely approximated by the experimental results of Groups 1 and 14, with the target bulk density aligning with Groups 1, 22, and 25. For sandy siltstone, the target compressive strength corresponds to Group 3, while the target bulk density closely matches the results of Groups 3, 9, 13, and 24. The target compressive strength of the lining concrete is closely approximated by the experimental results of Groups 15 and 21, whereas the target bulk density corresponds closely to Groups 6 and 21. Accordingly, siltstone was produced using Mix Group 4 (coal gangue: sand: cement: fly ash: graphite powder: steel fibres = 120:80:24:16:3:1), fine sandstone using Mix Group 1 (895:597:90:269:12:1), sandy siltstone using Mix Group 3 (225:150:38:38:4:1), and the lining concrete using Mix Group 21 (898:598:70:30:3:1), establishing the finalized similitude mix proportions for the physical model.

TABLE 5 presents the key mechanical parameters of the three similar materials, including their uniaxial compressive strength, elastic modulus, cohesion, and Poisson's ratio. A comparison of the data in TABLES 3 and 5 indicates that the measured mechanical properties of the prepared similar materials agree well with the theoretical target values converted from the original rock. The uniaxial compressive strength, elastic modulus, and Poisson's ratio were obtained through

indoor uniaxial compression tests. Due to limitations in the experimental conditions, the internal friction angle and tensile strength were not measured and are therefore not included in the table. Comprehensive analysis of the deformation and strength parameters demonstrates that the prepared similar materials can effectively reproduce the mechanical characteristics of the original rock and satisfy the requirements for material similarity in similar simulation tests.

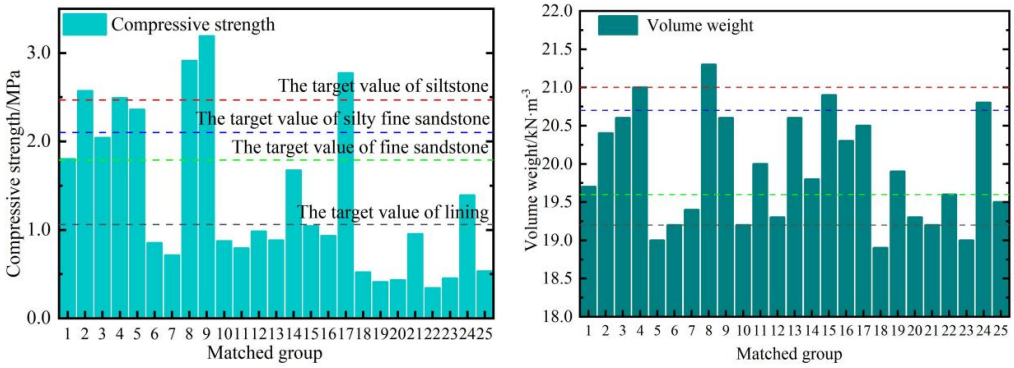

(a) Compressive strength (b) Volume weight

Fig. 4. Matching of similar materials

TABLE 5

Physical parameters of similar materials

Similar material Types	*E* /GPa	Cohesion /MPa	Poisson ratio
Siltstone	0.537	0.106	0.211
Fine sandstone	0.405	0.095	0.213
Silty fine sandstone	0.439	0.094	0.228

2.4. Model construction and monitoring scheme

Throughout the model assembly, pressure sensors, electrical resistivity electrodes, and distributed optical fibres were embedded to enable multi-source monitoring of stress, resistivity, and strain. Pressure sensors, comprising earth pressure cells and custom-fabricated strain bricks, were strategically embedded within the crown, invert, and arch shoulder regions of the chamber. Along the arch shoulders, the first sensor was located 5 cm from the outer lining surface, with a total of five sensors spaced at 5, 5, 10, and 10 cm intervals. In the crown and invert, the first sensor was also placed 5 cm from the lining exterior, with three sensors arranged at 5 and 10 cm intervals. The precise sensor arrangement is illustrated in Fig. 5(a). Electrical resistivity electrodes, consisting of 8 mm-diameter, 300 mm-long brass rods, were arranged around the lining in a square configuration with an 800 mm side length and 200 mm spacing, resulting in a total of 16 electrodes. The precise electrode positions are shown in Fig. 5(b). Additionally, distributed optical fibre sensors were helically installed along the surface of the lining model, with their specific arrangement depicted in Fig. 5(c).

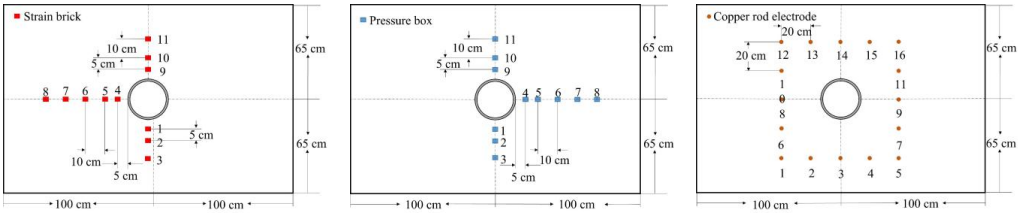

(a) Layout of strain brick (b) Layout of pressure box (c) Layout of copper rod electrode

Fig. 5. Physical model sensor embedment scheme

The model layers were sequentially arranged from top to bottom as 45 cm of fine sandstone, 50 cm of siltstone, and 45 cm of sandy siltstone. The tunnel lining was centrally located within the model, featuring an inner diameter of 25 cm and an outer diameter of 29 cm, ensuring proper representation of the prototype geometry. Owing to the substantial thickness of individual rock layers, a stratified layering approach was implemented. Using the previously established similar material mix designs for each lithology, the quantities of coal gangue, fine river sand, cement, fly ash, graphite powder, and steel fibres were computed, along with the thickness of each layer and the corresponding number of sub-layers. The detailed layering and material allocation are presented in TABLE 6.

TABLE 6

The amount of laying model materials and layering scheme

Lithology	Number	Material consumption /kg						Dimension /cm	Layer number
		Coal gangue	Sand	Cement	Fly ash	Graphite	Steel fibre		
Siltstone	4	656.40	437.60	131.28	87.52	13.41	2.47	45	9
Fine sandstone	1	652.05	434.94	65.57	195.98	15.74	2.73	50	10
Silty fine sandstone	3	644.33	429.55	108.82	108.82	12.45	2.36	45	10
Concrete lining	21	12.53	8.37	0.98	0.42	0.042	0.014	\	\

According to the determined material quantities and stratified layering plan, the materials for each layer of conductive concrete were accurately weighed, homogeneously mixed, and sequentially poured into the three-dimensional model setup. Following placement, each layer was densely compacted using a handheld vibration rod to ensure uniform consolidation. In the model construction process, the tunnel lining was fabricated separately using a double-layer cylindrical mould and positioned at the centre of the model. Subsequent layer placement ensured proper coupling between the lining and the surrounding rock. The detailed construction procedure of the physical model is shown in Fig. 6. Upon completion of the three-dimensional model assembly, the model was cured for 15 days to reach the intended strength.

Informed by the measured in-situ stress conditions of the prototype region, the model was incrementally subjected to vertical, horizontal, and axial loads of 0.78, 0.66, and 0.90 MPa, re-

spectively, until the design target loads for the experiment were achieved. After achieving load stabilisation, the surrounding rock-lining model was subjected to staged excavation, simulated by sequentially withdrawing the inner lining moulds. The model tunnel, with a total length of 70 cm, was excavated in seven discrete steps, ensuring controlled and reproducible excavation conditions. After the excavation of the model reached a stable state, a single-stage cyclic load ranging from 0.25 to 0.5 MPa was applied via a high-pressure airbag. Each cycle lasted 5 minutes, and a total of 50 cycles were conducted to investigate the response under repeated loading. Ultimately, the model was subjected to multi-stage cyclic loading using a hydraulic loading system, with upper-limit stresses incrementally increased from an initial 0.5 MPa in steps of 0.1 MPa until model failure occurred, as shown in Fig. 6. Real-time monitoring of multi-source physical parameters-including stress, deformation, and electrical resistivity-was conducted throughout the excavation and internal pressure loading stages to investigate the mechanical response and damage evolution of the tunnel lining structure under applied loads. In this physical model test, only the pressure effect during cyclic loading was considered. The temperature cyclic load induced by the thermodynamic effects of charging and discharging was not introduced. Temperature variations can generate thermal stress and promote crack propagation, thereby aggravating surrounding rock damage. However, the cyclic stress fluctuations caused by air pressure variations represent the primary controlling factor governing damage evolution in the chamber surrounding rock. Therefore, the test results can reflect the fundamental damage evolution characteristics under cyclic air pressure loading. In future studies, a thermo-mechanical coupling numerical model can be developed to further elucidate the temperature-stress coupling mechanism.

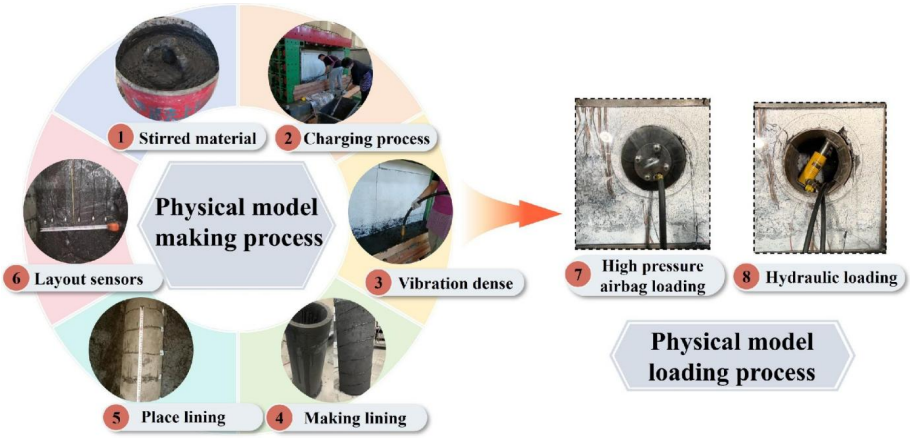

Fig. 6. Model building and loading procedure

3. Stress evolution characteristics

3.1. Stress evolution during the single-stage cyclic loading phase

The first-stage loading process primarily consists of three steps: application of the initial in-situ stress boundary, model excavation, and the application of a single-stage cyclic load using

a high-pressure airbag. The evolution characteristics of vertical and horizontal stresses in the surrounding rock-lining system during this stage are illustrated in Fig. 7.

(1) Fig. 7(a)-(d) depict the stress field adjustment process during excavation. Under the applied initial stress boundary, a relatively stable initial stress state is first established within the model. As excavation proceeds, the original stress equilibrium is disrupted, leading to stress redistribution in the surrounding rock and lining structure adjacent to the roadway. Along the measurement lines from shallow to deep regions, both the vertical stress at the roof and floor and the horizontal stress at the sidewalls exhibit varying degrees of stress release. The stress variations are more pronounced at shallow measurement points near the roadway contour, while changes in deeper surrounding rock are comparatively minor. This behaviour is primarily attributed to the release of radial constraints around the excavation boundary. In the roof and floor regions, the vertical direction is closely aligned with the radial stress direction; thus, excavation weakens the confinement in this direction, resulting in a reduction in vertical stress at the crown and invert. In contrast, for the sidewall regions, the horizontal direction corresponds to the principal radial stress direction, leading to a more significant release of horizontal stress following excavation unloading. Monitoring results indicate that the vertical stress at the roof and floor decreases by approximately 5.88%-22.39%, while the horizontal stress at the sidewalls decreases by about 6.52%-43.48%. These findings suggest that excavation-induced disturbances are primarily concentrated in the near-field region of the roadway and gradually attenuate with increasing distance from the excavation boundary.

The horizontal stress at the roof and floor, as well as the vertical stress at the sidewalls, exhibit a stepwise increasing trend during the excavation process. This phenomenon can be attributed to the release of radial stress around the excavation boundary, which causes part of the load to be redistributed and transferred to the tangential direction, thereby enhancing the tangential load-bearing effect and inducing stress concentration. Specifically, the horizontal stress at the roof and floor increases by approximately 10.75%-33.70%, while the vertical stress at the sidewalls increases by about 1.47%-26.47%. The stress growth rate demonstrates a clear spatial characteristic, with more pronounced increases in the near-field region of the roadway and relatively smaller changes in the deep surrounding rock, indicating that the excavation-induced stress redistribution attenuates with distance. In addition, the stress at each measurement point exhibits a stepwise variation during excavation, which is closely related to the staged advancement of the excavation process. Each excavation step alters the boundary constraints of the local surrounding rock, causing the stress field to undergo a cyclic process of "unloading-adjustment-rebalancing." Consequently, the stress evolution curves display features of abrupt stage-wise changes followed by gradual stabilisation. Overall, the stress response of the surrounding rock-lining system during the excavation stage is consistent with the fundamental mechanical behaviour of underground openings, characterised by radial stress release and tangential stress concentration after excavation.

(2) Fig. 8(a)-(d) illustrate the evolution characteristics of the model stress during the application of a single-stage cyclic load using a high-pressure airbag. Compared with the excavation stage, the stress variations at each measurement point under cyclic internal pressure are relatively smaller; however, noticeable differences in stress response still exist across different positions and directions. The roof region and shallow surrounding rock are more sensitive to stress disturbances, exhibiting pronounced periodic fluctuations in response to air pressure loading and unloading. In contrast, the stress variation at deeper measurement points is limited, indicating that the disturbance induced by internal pressure is primarily concentrated in the near-field region of the roadway and gradually attenuates as it propagates into the deeper surrounding rock.

During the high-pressure gas storage stage, the internal pressure of the airbag increases, which is equivalent to applying an outward radial pressure on the inner wall of the lining. This pressure partially compensates for the radial stress reduction caused by excavation unloading, leading to an increase in vertical stress at the roof and horizontal stress at the sidewalls. Monitoring results indicate that the vertical stress at the roof increases to 0.67-0.71 MPa, while the horizontal stress at the sidewalls rises to 0.62-0.86 MPa. Due to the adjustment of the stress state around the excavation boundary following the enhancement of radial support, part of the tangential stress is released. This is reflected in a decrease in horizontal stress at the roof to 1.00-1.15 MPa and a reduction in vertical stress at the sidewalls to 0.70-0.77 MPa.

During the low-pressure gas storage stage, the internal pressure of the airbag decreases, leading to a reduction in radial support on the inner wall of the lining. Consequently, the stress state around the excavation boundary adjusts to the lower internal pressure condition. At this stage, the vertical stress at the roof and the horizontal stress at the sidewalls decrease, while the

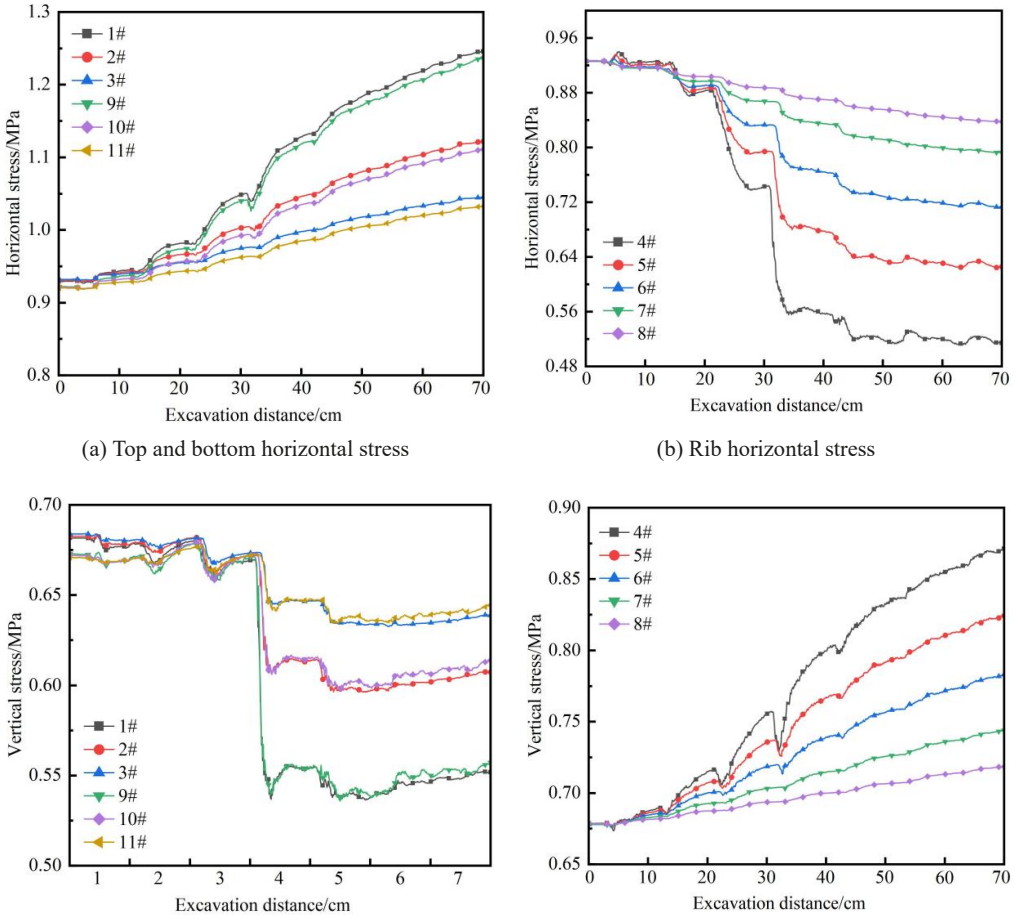

(a) Top and bottom horizontal stress

(b) Rib horizontal stress

(c) Top and bottom vertical stress

(d) Rib vertical stress

Fig. 7. The stress evolution law of different positions of the model in the excavation stage

horizontal stress at the roof and the vertical stress at the sidewalls increase to a certain extent. This behaviour indicates that alternating internal pressure primarily induces stress redistribution between radial and tangential components by modifying the radial support conditions of the lining inner wall. Under cyclic loading conditions with 0.5 MPa high-pressure gas storage and 0.25 MPa low-pressure gas storage, no abrupt stress increases or continuous cumulative growth are observed in the surrounding rock-lining structure. Instead, the stress at each measurement point fluctuates within a relatively small range. This suggests that, under the loading conditions of this stage, variations in internal pressure do not trigger significant instability in the surrounding rock-lining system. The stress response is dominated by recoverable elastic adjustment and localised redistribution, and the overall structure remains in a relatively stable state.

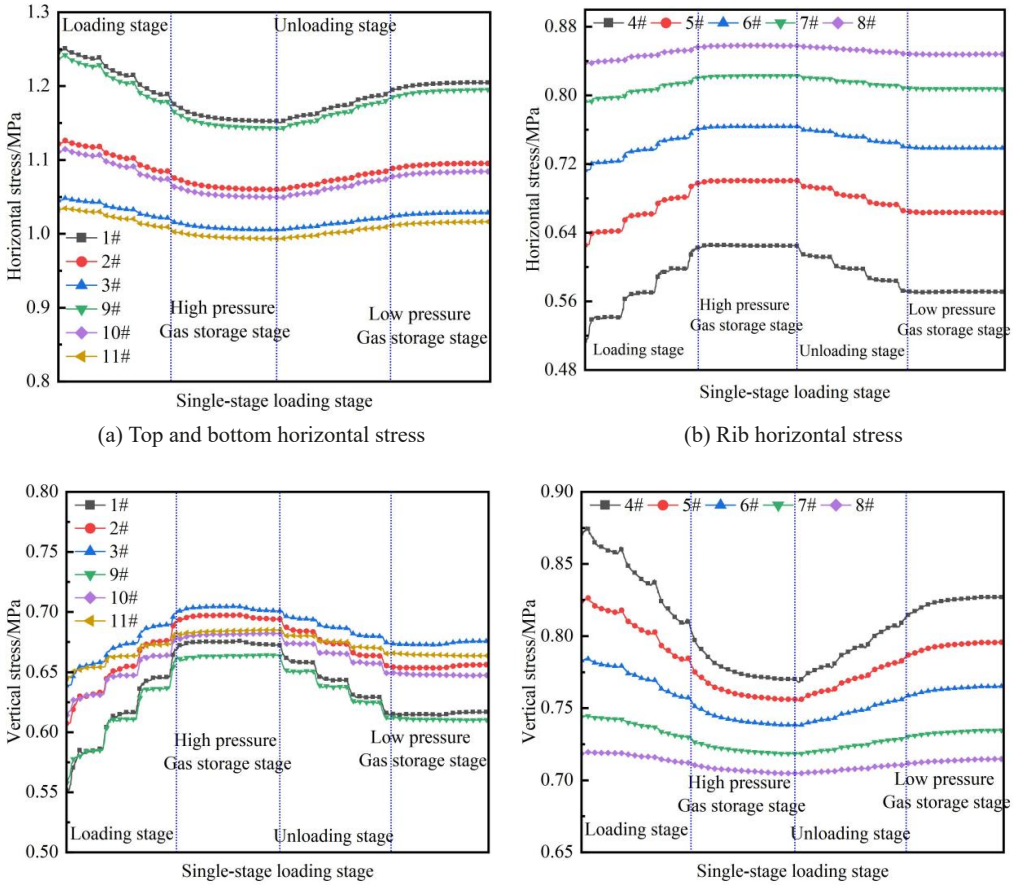

(a) Top and bottom horizontal stress

(b) Rib horizontal stress

(c) Top and bottom vertical stress

(d) Rib vertical stress

Fig. 8. Stress evolution law of the model at different positions

In conclusion, within the initial stress environment and under the combined effects of excavation-induced unloading and single-stage cyclic loading, stresses in the surrounding rock-lining

regions adjacent to the gas storage space decreased markedly, creating a stress-reduction zone. In contrast, stress concentrations formed in the deeper surrounding rock located farther from the lining structure. Moreover, under single-stage cyclic loading, the comparatively low upper-limit stress led to a marked attenuation of stress fluctuations relative to the excavation phase. The overall stress distribution stabilised, and no structural instability or failure was observed, even with increasing loading cycles.

3.2. Stress evolution during the graded cyclic loading phase

During the stage of graded cyclic loading, the stress distribution at different positions of the roof, floor, and sidewalls of the roadway is presented in Fig. 9. According to the results, initial failure of the model occurs when the upper limit of the cyclic load reaches 1.2 MPa. At this stage,

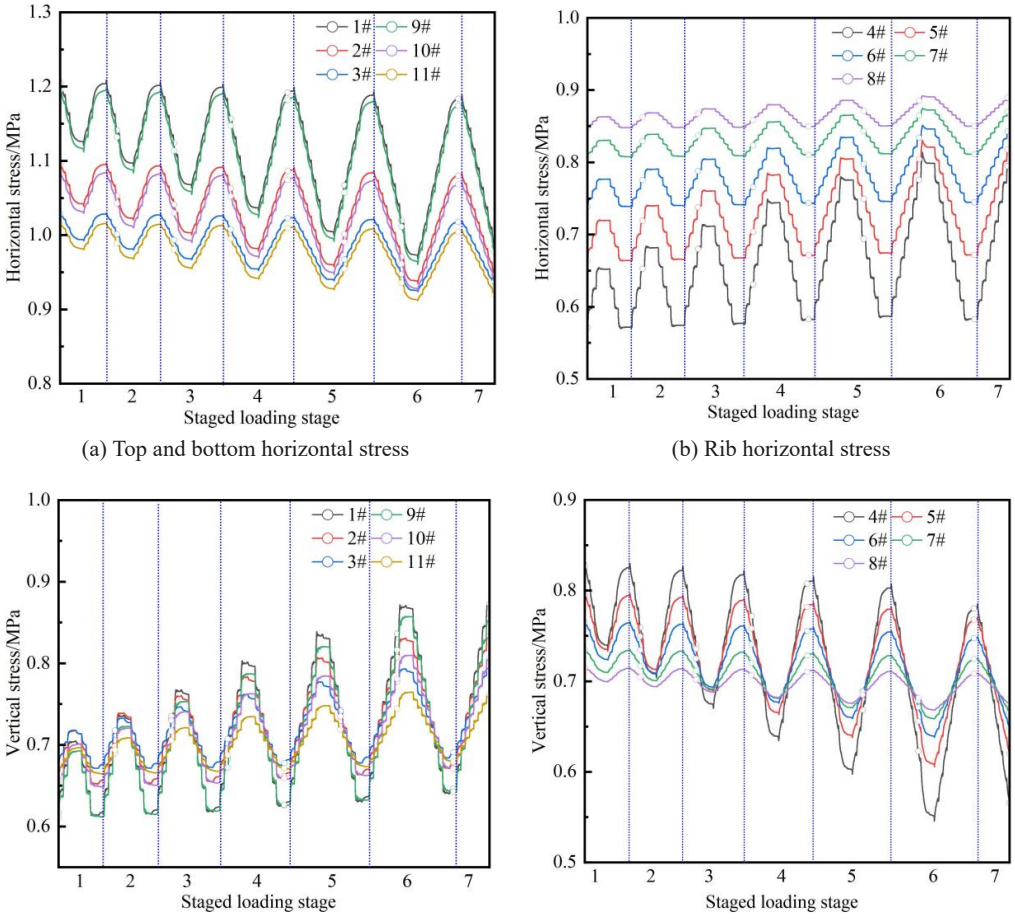

(a) Top and bottom horizontal stress

(b) Rib horizontal stress

(c) Top and bottom vertical stress

(d) Rib vertical stress

Fig. 9. The evolution of stress at different positions in the stage model of graded alternating internal pressure loading

the horizontal stress at the roof measuring points (Nos. 9, 10, and 11) decreases to 0.97 MPa, 0.94 MPa, and 0.92 MPa, respectively, representing reductions of 21.77%, 16.07%, and 11.54% compared with the post-excavation state. In contrast, the horizontal stress at the sidewall measuring points (Nos. 4-8) increases to 0.79 MPa, 0.82 MPa, 0.84 MPa, 0.87 MPa, and 0.89 MPa, corresponding to increases of 54.90%, 32.26%, 18.31%, 10.13%, and 5.95%, respectively. The vertical stress at the roof measuring points (Nos. 9-11) rises to 0.85 MPa, 0.81 MPa, and 0.76 MPa, with increases of 60.38%, 32.79%, and 18.75%, respectively. In contrast, the vertical stress at the sidewall measuring points (Nos. 4-8) decreases to 0.57 MPa, 0.62 MPa, 0.65 MPa, 0.67 MPa, and 0.68 MPa, corresponding to reductions of 33.72%, 24.39%, 16.67%, 8.22%, and 1.45%, respectively.

As the upper limit of the cyclic load increases progressively, the internal stress redistribution within the surrounding rock intensifies. Under the continuous disturbance of cyclic loading, the original horizontal load-bearing capacity at the roof is gradually weakened, leading to the continuous release and transfer of horizontal stress toward the sidewalls, thereby causing a sustained increase in horizontal stress at the sides. Simultaneously, the vertical load borne by the roof gradually increases, while the vertical stress at the sidewalls is redistributed toward the roof and deeper surrounding rock. This results in an increase in vertical stress at the roof and a corresponding decrease at the sidewalls. These observations indicate that, prior to the initial failure of the model, significant stress transfer and localised concentration have already developed within the surrounding rock mass, suggesting that the system has entered a transitional stage from elastic response to localised failure. The amplitude of stress variation at different measurement points decreases progressively with increasing distance from the lining, demonstrating a clear spatial attenuation effect of cyclic loading disturbance. The surrounding rock near the roadway contour is subjected to the combined effects of excavation unloading and cyclic loading, leading to the most pronounced stress adjustments. As the distance from the excavation boundary increases, the confinement effect of the surrounding rock mass becomes stronger, and stress redistribution gradually stabilises, resulting in significantly reduced stress variation amplitudes at deeper measurement points.

4. Strain evolution characteristics

4.1. Reconstruction method of the strain field in the composite structure

To capture the interface strain distribution of the surrounding rock-lining system, test optical fibres were pre-embedded at specific points along a spiral line on the outer lining surface (Fig. 10), with care taken during model assembly to maintain intimate coupling among the lining, the fibres, and the surrounding rock. During successive experimental stages, the spatial configuration of the surrounding rock-lining system evolved under combined internal and external pressures. The embedded optical fibres measured the tangential strain, $\varepsilon_q(\mathrm{s})$, along the fibre length at each spatial position s, reflecting the strain distribution within the coupled system. Optical fibres arranged along the surrounding rock-lining interface in uniform-pitch spirals were unrolled onto a two-dimensional plane. The spiral coordinates (x, y, z) were mapped to planar coordinates (c, z), allowing the tangential strain $\varepsilon_q(s)$ to be expressed as $\varepsilon_q(c, z)$, which enabled the reconstruction of

the interface strain field of the surrounding rock-lining system. Compared with traditional strain gauges, this method can reconstruct the quasi-continuous two-dimensional strain field of the interface by continuously acquiring strain information from the spiral optical fibre, combined with cylindrical expansion coordinate transformation and interpolation algorithms. It should be noted that the geometric coordinate mapping process introduces a small additional error; however, this error remains within an acceptable range for the regular cylindrical lining conditions considered in this model test. The advantage of this method does not lie in improving the accuracy of single-point measurements, but rather in enabling full-field strain characterisation of the surrounding rock-lining interface, thereby overcoming the limitations of discrete measurements using traditional strain gauges. Where c is the position coordinate of the circumference of the inner surface of the cross-section of the roadway, z is the position coordinate along the axial direction of the roadway after the lateral expansion of the interface, and β is the initial spiral angle of the optical fibre.

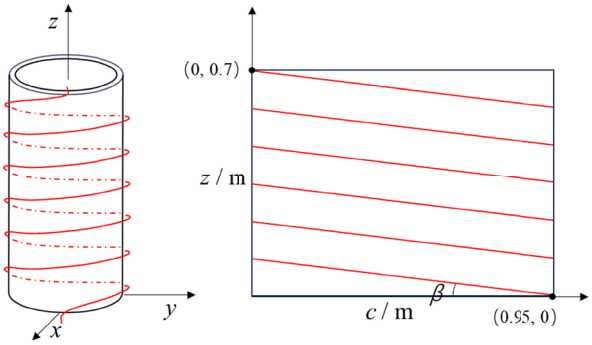

Fig. 10. Optical fibre layout at the interface of the surrounding rock and lining structure

From the geometric relationships, the transformation between coordinates can be formulated as:

$$\begin{cases} \dfrac{s}{c_0 / \cos(\beta)} = r....q \\ c = q\cos(\beta) \\ z = s\sin(\beta) \end{cases} \tag{8}$$

In this context, c_0 represents the circumference of the roadway cross-section at which the optical fibre is deployed; n is the integer quotient indicating the total number of spiral turns completed at the (c, z) position; and q is the remainder, corresponding to the residual length of the spiral after n turns at the (c, z) location. Using these definitions, the two-dimensional coordinates of any point along the spiral fibre can be determined. The strain measurements acquired from the optical fibres were associated with their corresponding transformed two-dimensional coordinates, resulting in a dense planar strain distribution. An interpolation algorithm was subsequently employed to reconstruct the planar strain field along the interface of the surrounding rock-lining system.

4.2. Strain field during the single-stage cyclic loading phase

The strain distribution characteristics of the surrounding rock-lining structure during excavation and single-stage cyclic loading are presented in Fig. 11. The results indicate the following:

1. During the excavation stage, the strain monitored by distributed optical fibre in the excavation section is initially less than 0, indicating that the surrounding rock-lining structure is dominated by compressive strain. This behaviour arises because excavation disrupts the original in-situ stress equilibrium, leading to stress redistribution within the surrounding rock. Under the continuous action of boundary stresses, loads are transferred to the periphery of the roadway, resulting in compressive deformation of the surrounding rock-lining structure within the excavation influence zone. In contrast, the unexcavated regions remain outside the stress adjustment range, and their stress state remains relatively stable, with only minor strain fluctuations. As the excavation advances, the influence range of unloading progressively expands, and the compressive strain zone propagates forward, exhibiting a clear staged distribution characteristic. Meanwhile, the initially excavated region undergoes sufficient stress adjustment, where strain gradually accumulates and tends toward stabilisation. The stabilised compressive strain is approximately –1000 με, indicating that a new stress equilibrium state is gradually established in the surrounding rock-lining system under boundary stress conditions.
2. At the initial stage of single-stage cyclic loading, the surrounding rock-lining structure remains dominated by compressive strain; however, the overall compressive strain is reduced compared with the excavation stage due to the effect of uniform internal pressure.

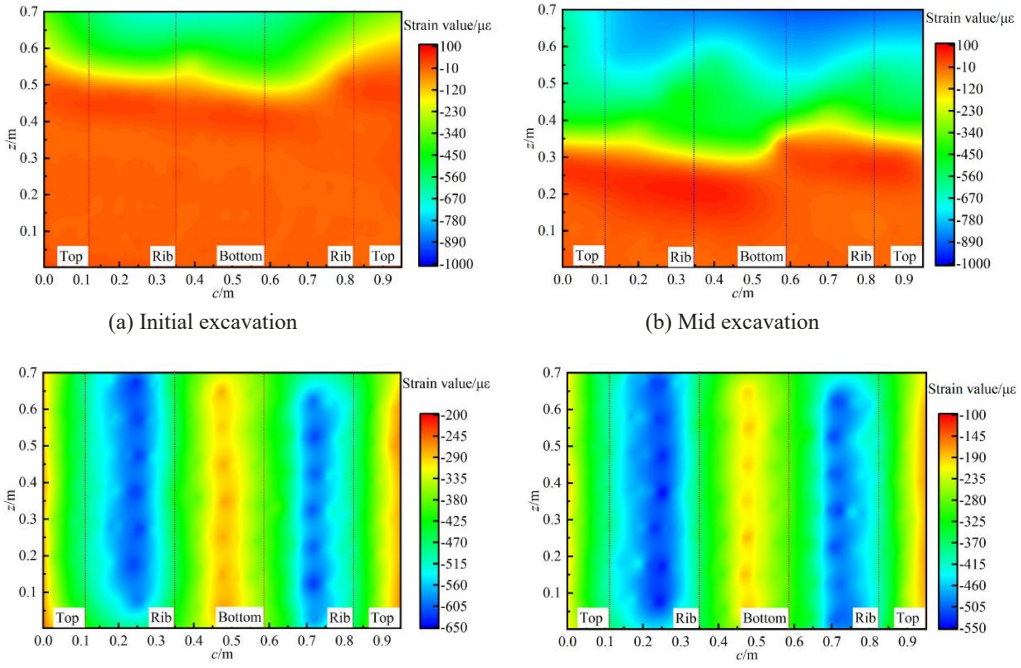

(a) Initial excavation

(b) Mid excavation

(c) Single-stage alternating load loading (n = 5)

(d) Single-stage alternating load loading (n = 45)

Fig. 11. Strain distribution characteristics during excavation and single-stage strain internal pressure loading

Specifically, the peak compressive strain in the sidewall regions is approximately –600 με, and the strain field exhibits a distinct distribution pattern characterised by "larger at the sides and smaller at the roof and floor." This phenomenon is closely associated with stress redistribution after excavation. The horizontal stress of the surrounding rock is primarily concentrated at the sidewalls, resulting in greater compressive loading and more pronounced deformation in these regions. In contrast, the stresses at the roof and floor are relatively lower, leading to smaller strain magnitudes, which reflects a good correspondence between the stress and deformation responses of the surrounding rock-lining structure.

3. With the cyclic action of alternating load, the peak compressive strain at the sidewalls is approximately –550 με, which is slightly lower than that observed at the initial loading stage, and the overall strain fluctuation remains limited. This indicates that, under a cyclic loading upper limit of 0.5 MPa, the applied load is insufficient to induce significant adjustment of the internal stress state of the surrounding rock-lining system. The deformation response is still dominated by elastic compressive behaviour, without evident accumulation of deformation, and the overall strain field remains relatively stable.

4.3. Strain field during the graded cyclic loading phase

The strain distribution characteristics of the surrounding rock-lining structure during the graded cyclic loading stage are presented in Fig. 12. As shown in the figure, with the progressive increase in the upper-limit stress of cyclic loading, the strain field undergoes a significant evolution, gradually transitioning from an overall compressive state to localised tensile behaviour. This reflects the continuous adjustment of the internal stress state of the structure. When the upper limit stress is 0.7 MPa, the surrounding rock-lining structure remains dominated by compressive deformation, with the most pronounced compression occurring at the sidewalls, where the peak strain is approximately −450 με. At this stage, although cyclic loading further alters the stress distribution, the overall mechanical behaviour is still governed by compressive load-bearing, and the structure maintains good stability. As the upper limit stress increases to 0.9 MPa, the strain in local regions of the roof and floor gradually transitions from compression to tension, with strain values changing from negative to positive. The peak tensile strain at the roof reaches approximately 200 με, while the compressive strain at the sidewalls decreases to about −200 με. This indicates that the continued increase in cyclic loading intensifies internal stress redistribution within the surrounding rock, gradually weakening the lateral confinement provided by the sidewalls. Consequently, the roof and floor assume greater deformation coordination, leading to a transition from compressive to tensile states in localised areas and signalling a shift in the structural stress regime.

When the upper limit stress exceeds 1.0 MPa, the surrounding rock-lining structure becomes dominated by tensile deformation. The peak tensile strain in the roof and floor regions further increases to 700-1000 με. Meanwhile, more localised strain concentration zones emerge, and the uniformity of the strain distribution decreases significantly. These observations indicate that, with the continuous increase in cyclic loading, the internal stress adjustment becomes more pronounced, the deformation coordination capacity of local regions progressively deteriorates, and strain increasingly concentrates in localised areas. As a result, the structure enters a stage of instability evolution, with a markedly increased risk of failure.

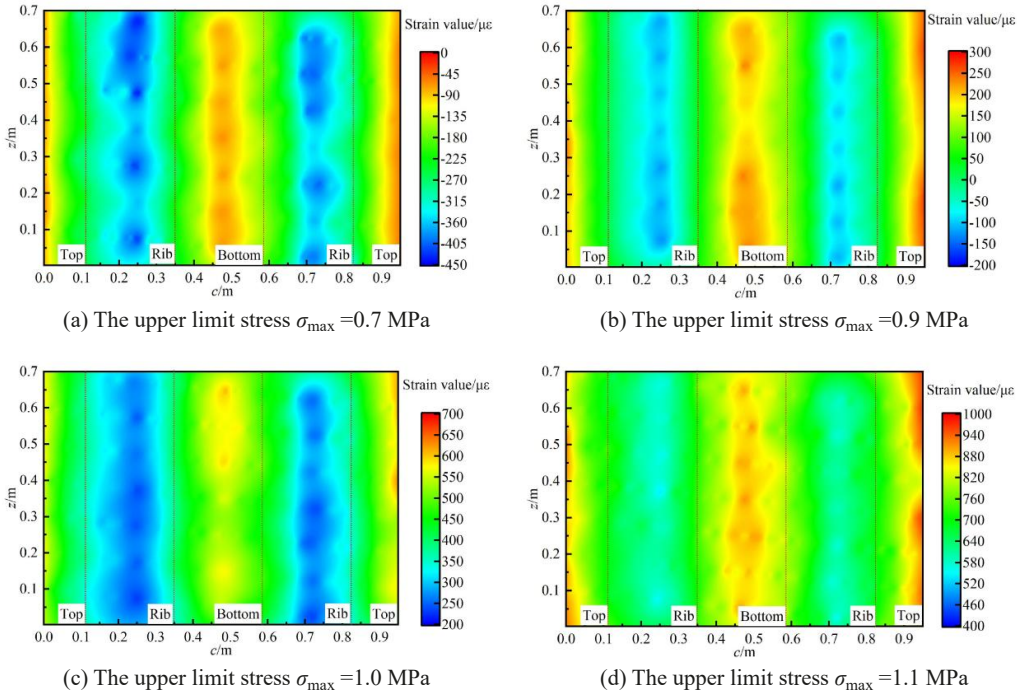

(a) The upper limit stress σ_{max} =0.7 MPa

(b) The upper limit stress σ_{max} =0.9 MPa

(c) The upper limit stress σ_{max} =1.0 MPa

(d) The upper limit stress σ_{max} =1.1 MPa

Fig. 12. Strain distribution characteristics during graded strain internal pressure loading stage

5. Damage instability characteristics

By analysing the strength degradation and resistivity variations of specimens with different conductive material contents before and after failure, a schematic representation of the micro-damage mechanism of conductive concrete under load was developed (Fig. 13). This schematic elucidates the evolution of conductive pathways throughout the loading process and failure, highlighting the mechanical mechanism whereby stress-induced changes in the micro-porous structure cause the disruption of conductive channels. During the initial stage of stress application, pores within the conductive concrete are randomly distributed, directly affecting the formation and scale of conductive pathways. As stress increases, the specimens gradually densify, pore volume decreases, and conductive phases form interconnected networks, resulting in enhanced electrical conductivity. With further deformation and damage, the pores enlarge and multiply, evolving into microcracks that compromise the conductive pathways and decrease the overall conductivity of the specimens. Once the macroscopic structure of the conductive concrete reaches its load-bearing capacity, large pores expand further and interconnect, forming macroscopic fracture surfaces. Structural instability occurs, internal conductive pathways are destroyed, and overall conductivity is further reduced. The regions near these macroscopic fracture surfaces, characterised by dense distributions of large pores, represent high-resistivity damage zones.

Based on the apparent resistivity data obtained from the built-in analyser of the WBD parallel electrical testing system, combined with the corresponding survey line coordinates and

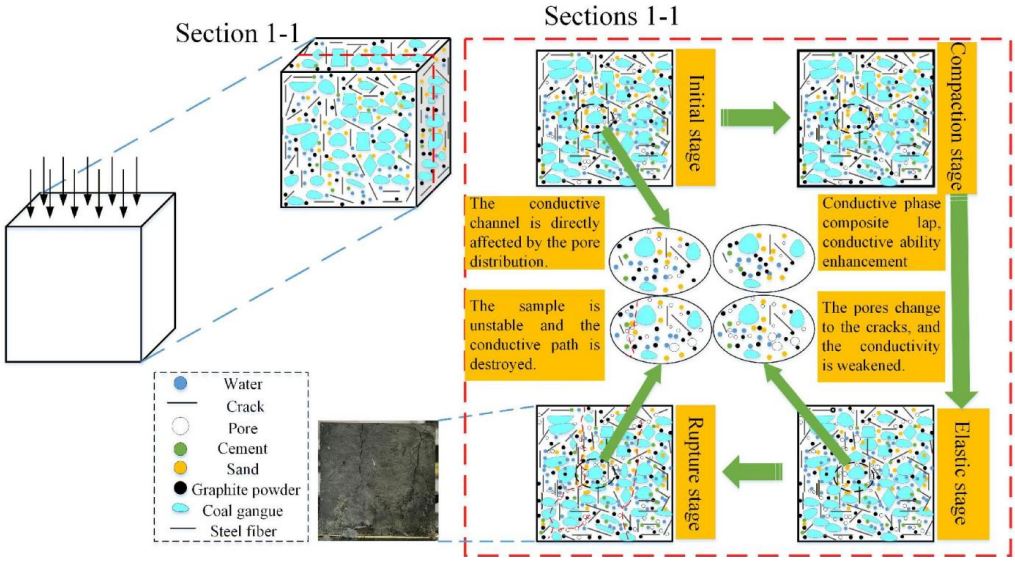

Fig. 13. Damage mechanism of conductive concrete and evolution mechanism of conductive channel

roadway contour coordinates, the AGI analysis software was used to perform data inversion and optimisation. The inversion results were subsequently visualised using plotting software. Due to the direct influence of the model preparation method (the reserved roadway lining), the initial apparent resistivity profile exhibits distinct zoning characteristics. Specifically, the preset roadway area presents relatively higher apparent resistivity, whereas the surrounding regions exhibit a layered distribution characterised by lower apparent resistivity. It should be noted that the detection resolution of apparent resistivity in deeper regions is constrained by electrode arrangement conditions. Based on real-time monitoring of the apparent resistivity response profiles, the evolution characteristics of apparent resistivity within the surrounding rock-lining structure during the initial model state and subsequent loading process can be obtained, as shown in Fig. 14.

Fig. 14(a) indicates that, after the application of boundary stresses, the conductive concrete specimens demonstrated a high degree of resistivity homogeneity, with apparent resistivity values remaining in the relatively low range of 100-200 Ω·m. Following the completion of gas storage chamber excavation (Fig. 14(b)), apparent resistivity in the shallow areas of the crown, invert, and lateral shoulders markedly increased. This observation suggests that the combined influence of boundary stress and excavation-induced unloading led to micro-damage and interconnected cracks in the shallow surrounding rock-lining system, thereby compromising the conductive pathways in these regions.

Following the completion of excavation, the system underwent single-stage cyclic loading using the high-pressure airbag (Fig. 14(c)). During this phase, cracks in the shallow surrounding rock-lining zones were partially compacted and closed under internal pressure, facilitating the reformation of conductive pathways and resulting in a decrease in apparent resistivity within these regions. Nevertheless, cracks in the deeper portions of the surrounding rock did not close, with resistivity remaining similar to the post-excavation state. Upon entering the single-stage cyclic unloading phase (Fig. 14(d)), cracks in the shallow regions previously compacted by the airbag

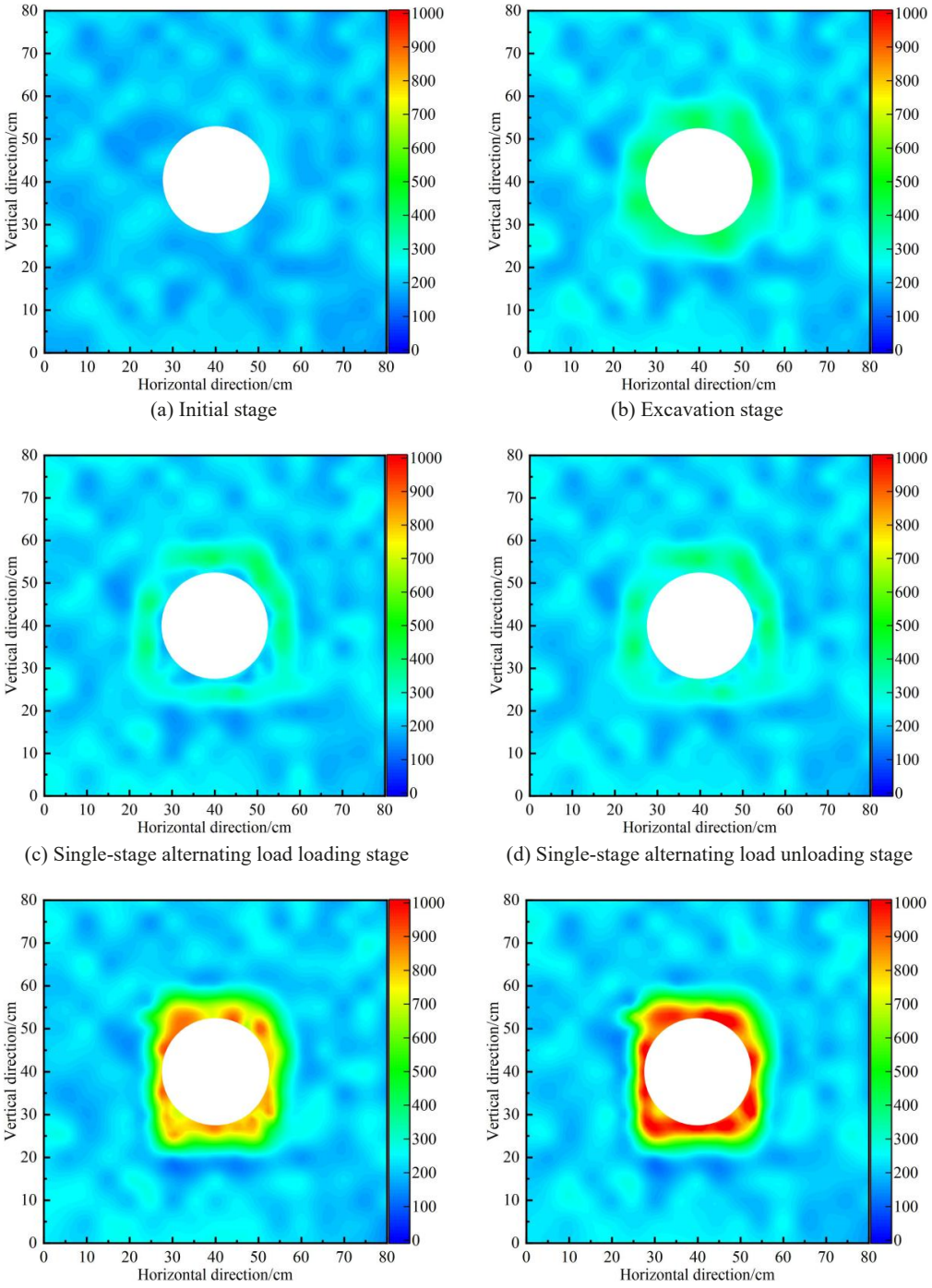

(a) Initial stage

(b) Excavation stage

(c) Single-stage alternating load loading stage

(d) Single-stage alternating load unloading stage

(e) Grading alternating load loading stage

(f) Failure stage

Fig. 14. Apparent resistivity response characteristics of the model during the test

reopened, leading to the destruction of conductive pathways and a corresponding increase in apparent resistivity in the shallow surrounding rock-lining system. During the multi-stage cyclic loading phase (Fig. 14(e)), as the upper-limit stress increased, microcracks within the surrounding rock-lining system continued to develop, resulting in clearly defined high-resistivity damage zones (resistivity > 800 Ω·m) in the shallow regions of the crown, invert, and arch shoulders. In the multi-stage cyclic unloading phase (Fig. 14(f)), apparent resistivity in the shallow zones of the surrounding rock-lining system continued to rise, with the high-resistivity damage zone expanding in area, though its radial extent remained largely unchanged. At this stage, failure of the roadway lining under elevated internal pressure, combined with the strength disparity between the lining and surrounding rock, restricted crack propagation to the lining layer, resulting in localised structural failure without extension into the deeper surrounding rock.

Taken together, the evolution of apparent resistivity responses clearly captured the progressive development of internal cracks in the model under cyclic loading, closely matching the observed failure patterns of the physical specimens. These results confirm the reliability of apparent resistivity measurements for monitoring damage evolution in surrounding rock-lining structures.

6. Conclusions

Utilising a multifunctional experimental platform and a multi-source monitoring system developed for deep mining engineering, this study provides an in-depth analysis of stress evolution, interface strain distribution, and damage-failure behaviour of surrounding rock-lining structures in decommissioned coal mine gas storage chambers under single-stage and multi-stage cyclic loading conditions. The key findings are summarised as follows:

(1) Under boundary stress conditions, unloading during excavation led to progressive stress relief of the vertical stresses at the crown and invert of the lining, as well as the arch shoulder stresses, along the sensor layout from shallow to deep. With the advancement of excavation stages, the extent of stress relief displayed a pronounced stepwise reduction trend. Concurrently, the horizontal stresses at the crown and invert of the model, as well as the vertical stresses at the arch shoulders, showed a distinct stepwise increase during the excavation process. Stress concentrations were observed at the roadway crown and in the deeper regions of the arch shoulders.

(2) The stress distribution of the surrounding rock-lining structure displayed periodic oscillations in response to single-stage and multi-stage cyclic loading. With increasing upper-limit stress, the extent to which the model stress distribution was affected gradually intensified, indicating a strong dependency of stress behaviour on the magnitude of the applied cyclic load. Pronounced stress variations were detected at multiple locations near the lining along the roadway crown and arch shoulders. Nevertheless, the magnitude of these variations progressively decreased with increasing distance from the lining, indicating a spatial attenuation of stress influence.

(3) Throughout the excavation and single-stage strain-controlled internal pressure loading, the deformation of the surrounding rock-lining system was primarily compressive. The structure displayed a clear zonal behaviour as a result of the post-excavation internal stress evolution, with the arch shoulders undergoing more pronounced compressive deformation compared to the crown and invert regions. With increasing upper-limit

stress during the multi-stage strain-controlled internal pressure loading, the deformation behaviour of the structure progressively shifted from compressive to tensile. Beyond an upper-limit stress of 1.0 MPa, the deformation of the surrounding rock-lining system became primarily tensile. Peak strain values at the crown and invert regions further increased to 700-1000 με, while additional localised heterogeneities in deformation appeared, signalling a heightened risk of structural instability.

(4) A micro-mechanical degradation mechanism of conductive concrete under load was proposed. Using apparent resistivity response profiles of the model at various internal pressure loading stages, the study provides a detailed account of the initial state and the evolution of apparent resistivity throughout the loading process. As the upper-limit stress of the cyclic loading increased, microcracks in the lining structure continued to develop, resulting in clearly defined high-resistivity damage zones in the shallow areas of the crown, invert, and arch shoulders. The apparent resistivity responses provided an effective indicator of the evolution of internal cracks and the damage-instability behaviour of the model throughout the different loading stages.

Acknowledgment

This work was supported by the Anhui Engineering Research Center of Exploitation and Utilization of Closed/Abandoned Mine Resources (No. EUCMR202301).

References

[1] L. Yuan, T. Zhang, Y.H. Wang, X.Z. Wang, Y.T. Wang, X.J. Hao, Scientific problems and key technologies for safe and efficient mining of deep coal resources. J. China Coal Soc. **50** (1), 1-12 (2025). DOI: https://doi.org/10.13225/j.cnki.jccs.YG25.0016

[2] K. Yang, L. Yuan,T. Wang, X.F. Yi, L.L. Zhang, K. Liu, Y.L. Huang, Q.R. Xiong, Y.Z. Jia, T.T. Wang, J.Z. Han, Research progress on detection-evaluation-utilization technology of deep special space. J. China Coal Soc. **51** (1), 689-720 (2026). DOI: https://doi.org/10.13225/j.cnki.jccs.2025.1059

[3] S. Plaatjie, M.S.D. Manzi, L. Linzer, M. Sihoyiya, Using 3D numerical simulations to model active in-mine seismic surveys at South Deep Gold Mine, South Africa. J. South. Afr. Inst. Min. Metall. **125** (1), 43-50 (2025). DOI: https://doi.org/10.17159/2411-9717/3473/2025

[4] R. Zhuo, P. Zhao, X. Sun, S. Li, H. Liu, Y.Y. Jia, L.L. Wang, Y.J. Liu, A COMSOL simulation of fracture-stress-seepage coupling during extremely thick coal seam mining. Eng. Fract. Mech. **326**, 111407 (2025). DOI: https://doi.org/10.1016/j.engfracmech.2025.111407

[5] Q. Ran, Y.P. Liang, C.F. Ye, Y.H. Ning, T.F. Ma, F.J. Kong, Failure analysis of overlying strata during inclined coal seam mining: Insights from acoustic emission monitoring. Eng. Fail. Anal. **182**, 110023 (2025). DOI: https://doi.org/10.1016/j.engfailanal.2025.110023

[6] L.G. Jia, Experimental Study on the Failure Characteristics of Strata with Different Filling Rates in Long-wall Filling Mining. E3S Web Conf. **53**, 03043 (2018). DOI: https://doi.org/10.1051/e3sconf/20185303043

[7] X.S. Liu, S.L. Song, Y.L. Tan, D.Y. Fan, J.G. Ning, X.B. Li, Y.C. Yin, Similar simulation study on the deformation and failure of surrounding rock of a large section chamber group under dynamic loading. Int. J. Min. Sci. Technol. **31** (3), 495-505 (2021). DOI: https://doi.org/10.1016/j.ijmst.2021.03.009

[8] X.S. Li, S. Yang, Y.M. Wang, W. Nie, Z.F. Liu, Macro-Micro Response Characteristics of Surrounding Rock and Overlying Strata towards the Transition from Open-Pit to Underground Mining. Geofluids **2021** (1), 5582218 (2021). DOI: https://doi.org/10.1155/2021/5582218

[9] J. Zhang, Z. Wang, Z. Song, Numerical study on movement of dynamic strata in combined open-pit and underground mining based on similar material simulation experiment. Arab. J. Geosci. **13**, 785 (2020). DOI: https://doi.org/10.1007/s12517-020-05766-0

[10] K.Y. Yang, S.H. Li, K.Z. Xia, C.X. Chen, W.L. Shen, K. Deng, Large-Scale Failure Mechanism of a Footwall with Steeply Inclined Discontinuities in a Sublevel Caving Mine. Int. J. Geomech. **24** (8), 05024007 (2024). DOI: https://doi.org/10.1061/ijgnai.gmeng-9852

[11] H. Chen, W.Z. Ren, Development of epoxy-silicone rubber-based geotechnical similar material and its engineering application. Mater. Res. Innov. **19** (sup. 5), S5-296-S5-300 (2016). DOI: https://doi.org/10.1179/1432891714Z.0000000001096

[12] Z.H. Zhou, Z.Q. Chen, C. He, H. Kou, Investigation on the evolution characteristics and transfer mechanism of surrounding rock pressure for a hard-rock tunnel under high geo-stress: case study on the Erlang Mountain Tunnel, China. Bull. Eng. Geol. Environ. **80** (11), 8339-8361 (2021). DOI: https://doi.org/10.1007/s10064-021-02439-4

[13] Y. Li, Z. Yang, T. Wu, Discussion on the water-preserved coal mining by dewatering-reflooding water curtain in open-pit coal mines. Coal Geol. Explor. **49** (6), 160-166 (2021). DOI: https://doi.org/10.3969/j.issn.1001-1986.2021.06.019

[14] J.X. Shao, L.J. You, Y.L. Kang, X.P. Gao, M.J. Chen, S. Meng, N. Zhang, Experimental study on stress sensitivity of underground gas storage. J. Pet. Sci. Eng. **195**, 107577 (2020). DOI: https://doi.org/10.1016/j.petrol.2020.107577

[15] Z.L. She, B. Wang, Y. Zhang, L.F. Zeng, L.J. Xie, S.H.R. Shen, Study on Coal Seam Roof Failure Based on Optical Fiber Acoustic Sensing and the Parallel Electrical Method. Energies **17** (21), 5471 (2024). DOI: https://doi.org/10.3390/en17215471

[16] X.Y. Zhan, L. Gao, F.H. Zhao, Y.Y. Wang, P. Liu, S. Han, Experimental study on proportioning of ultra-high strength similar materials for large similarity ratio model tests. Coal Geol. Explor. **51** (11), 109-118 (2023). DOI: https://doi.org/10.12363/issn.1001-1986.23.05.0237

[17] Z.D. Lei, Z.G. Yan, Experimental Study on Proportioning of Similar Materials for Surrounding Rock of Class III, Chin. J. Undergr. Space Eng. **18** (3), 832-839 (2022). DOI: https://doi.org/10.20174/j.juse.2022.03.015

[18] B.X. Jia, W.Y. Yuan, C.Y. Ma, F.P. Liu, J.J. Zhang, Ratio test and characteristic analysis of similar materials in white sand rock. Chin. J. Undergr. Space Eng. **18** (2), 503-512 (2022). DOI: https://doi.org/10.20174/j.juse.2022.02.018

[19] Y.L. Liu, W.Z. Zhou, B. Guo, Q. Ma, H.L. Xiao, Study on marl similar materials in similar simulation test. Chin. J. Rock Mech. Eng. **39** (S1), 2795-2803 (2020). DOI: https://doi.org/10.13722/j.cnki.jrme.2019.0885

[20] X.Y. Zhang, L. Luo, L.F. Xu, M. Zhao, Research on quantitative determination method of similar materials ratio. Saf. Coal Mines **50**, 45-53 (2019). DOI: https://doi.org/10.13347/j.cnki.mkaq.2019.10.010

[21] P.F. Jiao, X. Zhang, X.Z. Li, B.H. Liu, H.J. Zhang, Experimental Study on the Ratio of Similar Materials in Weak Surrounding Rock Based on Orthogonal Design J. Eng. **2018**, 1-6 (2018). DOI: https://doi.org/10.1155/2018/2591758

[22] Q.Z. Wang, H.W. Ye, N. Li, G.F. Ren, T. Lei, D.F. Chen, W. Chen, Proportioning experiment and strength variation law of similar simulation materials for soft rock of coal measures Experimental Technology and Management **38** (9), 77-82 (2021). DOI: https://doi.org/10.16791/j.cnki.sjg.2021.09.015

[23] C.X. Zhu, X. Liu, W.H. Zhao, Study on the optimum proportioning of coal rock similar materials based on orthogonal experiment Journal of Henan Polytechnic University (Natural Science) **43** (2), 34-40 (2024). DOI: https://doi.org/10.16186/j.cnki.1673-9787.2022090049

[24] L.J. Sun, B.N. Wei, Experimental study on similar material ratio based on IBM SPSS statistical analysis, China Mining Magazine 33 (S2), 351-356 (2024). DOI: https://doi.org/10.12075/j.issn.1004-4051.20241932

[25] W.B. Zhu, B.Z. Zhao, S. Ning, J.H. Xiang, Characterization methods and experimental study of mining-induced rock mass damage and fracture using carbon fiber similar materials. Coal Science and Technology **53** (7), 70-80 (2025). DOI: https://doi.org/10.12438/cst.2025-0176

[26] J.G. Lu, X.L. Yang, W.L. Pu, X.S. Wan, Y.D. Wang, L.L. Tan, Current status and prospects of research on conductive concrete in cold regions. J. Civil Environ. Eng. **47** (2), 162-173 (2025). DOI: https://doi.org/10.11835/j.issn.2096-6717.2023.032

[27] R. Siddique, Utilization of cement kiln dust (CKD) in cement mortar and concrete-an overview. Resour. Conserv. Recycl. **48** (4), 315-338 (2006). DOI: https://doi.org/10.1016/j.resconrec.2006.03.010

[28] Y.X. Wu, J.W. Zhang, Y.D. Ai, W.C. Quan, Y.W. Gong, K.M. Yang, J. Gao, L. Li, C.W. Hao, W.B. Li, W.J. Ai, K. Yang, H.G. Cheng, Effect of freeze-thaw cycles on nitrogen retention in an alpine topsoil amended with peanut shell hydrochar. Environ. Res. **289**, 123342 (2026).
DOI: https://doi.org/10.1016/j.envres.2025.123342

[29] Z.H. Ren, H. Zeng, X.T. Zeng, X. Chen, X.Y. Wang, Effect of Nanographite Conductive Concrete Mixed with Magnetite Sand Excited by Different Alkali Activators and Their Combinations on the Properties of Conductive Concrete. Buildings **13** (7), 1630 (2023). DOI: https://doi.org/10.3390/buildings13071630

[30] Q.C. Chen, X.D. Kong, J.K. Chen, Stability study of piezoresistive effect of conductive concrete under freeze-thaw cycles. Journal of Ningbo University (Natural Science & Engineering Edition) **35** (5), 54-63 (2022).
DOI: https://doi.org/10.3969/j.issn.1001-5132.2022.05.007

[31] A. Malakooti, H. Abdualla, S. Sadati, H. Ceylan, S. Kim, K. Cetin, Experimental and theoretical characterization of electrodes on electrical and thermal performance of electrically conductive concrete. Compos. B: Eng. **222**, 109003 (2021). DOI: https://doi.org/10.1016/j.compositesb.2021.109003

[32] X.D. Kong, J.K. Chen, Study on Thermal Deformation and Astuteness of Conductive Concrete Sensors. Chinese Journal of Solid Mechanics **42** (6), 642-655 (2021).
DOI: https://doi.org/10.19636/j.cnki.cjsm42-1250/o3.2021.025

[33] Y.H. Li, Study on preparation of conductive concrete and its mechanical and conductive properties. Protective Engineering **42** (3), 26-31 (2020). DOI: https://doi.org/10.3969/j.issn.1674-1854.2020.03.004

[34] Z.G. Yao, H. Luo, J.Y. He, K.C. Ying, T. Yu, Y. Fang, Integration of multi-physical signals for monitoring shear failure in jointed granite: insights from experimental study. Bull. Eng. Geol. Environ. **84**, 409 (2025).
DOI: https://doi.org/10.1007/S10064-025-04438-1